

The unexpected uses of a bowling pin: anisotropic flow in fixed-target $^{208}\text{Pb}+^{20}\text{Ne}$ collisions as a probe of quark-gluon plasma

Giuliano Giacalone,^{1,*} Wenbin Zhao,^{2,3,†} Benjamin Bally,⁴ Shihang Shen,⁵

Thomas Duguet,^{6,7} Jean-Paul Ebran,^{8,9} Serdar Elhatisari,¹⁰ Mikael Frosini,¹¹

Timo A. Lähde,^{12,13} Dean Lee,¹⁴ Bing-Nan Lu,¹⁵ Yuan-Zhuo Ma,¹⁴ Ulf-G. Meißner,^{16,17,5}

Govert Nijs,¹⁸ Jacquelyn Noronha-Hostler,¹⁹ Christopher Plumberg,²⁰ Tomás R. Rodríguez,²¹

Robert Roth,^{22,23} Wilke van der Schee,^{18,24,25} Björn Schenke,^{26,‡} Chun Shen,^{27,28,§} and Vittorio Somà⁶

¹*Institut für Theoretische Physik, Universität Heidelberg, Philosophenweg 16, 69120 Heidelberg, Germany*

²*Nuclear Science Division, Lawrence Berkeley National Laboratory, Berkeley, California 94720, USA*

³*Physics Department, University of California, Berkeley, California 94720, USA*

⁴*ESNT, IRFU, CEA, Université Paris-Saclay, 91191 Gif-sur-Yvette, France*

⁵*Institute for Advanced Simulation (IAS-4), Forschungszentrum Jülich, D-52425 Jülich, Germany*

⁶*IRFU, CEA, Université Paris-Saclay, 91191 Gif-sur-Yvette, France*

⁷*KU Leuven, Instituut voor Kern- en Stralingsfysica, 3001 Leuven, Belgium*

⁸*CEA, DAM, DIF, 91297 Arpajon, France*

⁹*Université Paris-Saclay, CEA, Laboratoire Matière en Conditions Extrêmes, 91680 Bruyères-le-Châtel, France*

¹⁰*Faculty of Natural Sciences and Engineering, Gaziantep Islam Science and Technology University, Gaziantep 27010, Turkey*

¹¹*CEA, DES, IRESNE, DER, SPRC, LEPH, 13115 Saint-Paul-lez-Durance, France*

¹²*Institut für Kernphysik, Institute for Advanced Simulation and Jülich Center for Hadron Physics, Forschungszentrum Jülich, D-52425 Jülich, Germany*

¹³*Center for Advanced Simulation and Analytics (CASA),*

Forschungszentrum Jülich, D-52425 Jülich, Germany

¹⁴*Facility for Rare Isotope Beams and Department of Physics and Astronomy, Michigan State University, MI 48824, USA*

¹⁵*Graduate School of China Academy of Engineering Physics, Beijing 100193, China*

¹⁶*Helmholtz-Institut für Strahlen- und Kernphysik, Universität Bonn, D-53115 Bonn, Germany*

¹⁷*Bethe Center for Theoretical Physics, Universität Bonn, D-53115 Bonn, Germany*

¹⁸*Theoretical Physics Department, CERN, CH-1211 Genève 23, Switzerland*

¹⁹*Illinois Center for Advanced Studies of the Universe, Department of Physics, University of Illinois at Urbana-Champaign, Urbana, IL 61801, USA*

²⁰*Natural Science Division, Pepperdine University, Malibu, CA 90263, USA*

²¹*Departamento de Estructura de la Materia, Física Térmica y Electrónica and IPARCOS, Universidad Complutense de Madrid, E-28040 Madrid, Spain*

²²*Institut für Kernphysik, Technische Universität Darmstadt, 64289 Darmstadt, Germany*

²³*Helmholtz Forschungsakademie Hessen für FAIR,*

GSI Helmholtzzentrum, 64289 Darmstadt, Germany

²⁴*Institute for Theoretical Physics, Utrecht University, 3584 CC Utrecht, The Netherlands*

²⁵*NIKHEF, Amsterdam, The Netherlands*

²⁶*Physics Department, Brookhaven National Laboratory, Upton, NY 11973, USA*

²⁷*Department of Physics and Astronomy, Wayne State University, Detroit, Michigan 48201, USA*

²⁸*RIKEN BNL Research Center, Brookhaven National Laboratory, Upton, NY 11973, USA*

The System for Measuring Overlap with Gas (SMOG2) at the LHCb detector enables the study of fixed-target ion-ion collisions at relativistic energies ($\sqrt{s_{NN}} \sim 100$ GeV in the centre-of-mass). With input from *ab initio* calculations of the structure of ^{16}O and ^{20}Ne , we compute 3+1D hydrodynamic predictions for the anisotropic flow of Pb+Ne and Pb+O collisions, to be tested with upcoming LHCb data. This will allow the detailed study of quark-gluon plasma (QGP) formation as well as experimental tests of the predicted nuclear shapes. Elliptic flow (v_2) in Pb+Ne collisions is greatly enhanced compared to the Pb+O baseline due to the shape of ^{20}Ne , which is deformed in a bowling-pin geometry. Owing to the large ^{208}Pb radius, this effect is seen in a broad centrality range, a unique feature of this collision configuration. Larger elliptic flow further enhances the quadrangular flow (v_4) of Pb+Ne collisions via non-linear coupling, and impacts the sign of the kurtosis of the elliptic flow vector distribution ($c_2\{4\}$). Exploiting the shape of ^{20}Ne proves thus an ideal method to investigate the formation of QGP in fixed-target experiments at LHCb, and demonstrates the power of SMOG2 as a tool to image nuclear ground states.

Over the past decades, collider experiments with atomic nuclei have enabled the exploration of the phase diagram of strong-interaction matter over a wide range of temperature and densities. At ultra-relativistic energies, experiments at the Relativistic Heavy Ion Col-

lider (RHIC) and at the CERN Large Hadron Collider (LHC) have established the formation of quark-gluon plasma (QGP) [1], the hot phase of QCD behaving like a near-ideal fluid of deconfined partons, via the observation of anisotropic flow [2] in combination with the

modification of hard probes due to their interaction with the hot environment [3]. At these energies, anisotropic flow signals persist down to small systems [4–7], including $p+p$, $\gamma+Pb$, and e^+e^- collisions [8–13], although without any visible hard-probe modification, leaving the question of the formation of QGP up to debate [14, 15]. Consequently, research on small systems has shed light on the apparent hydrodynamization of out-of-equilibrium QCD matter [16, 17]. In parallel, the Beam Energy Scan (BES) at RHIC has elucidated the equation of state and the transport properties of the QGP towards high net-baryon density [18–20], while fixed-target experiments close to the GeV scale have demonstrated the dominance of hadronic degrees of freedom and opened connections with the physics of neutron stars [21–23]. This wealth of experimental measurements in combination with advanced Bayesian inference methods [24–28] has helped shape a picture of nuclear matter gradually acquiring consistency across experiments and theoretical results.

To add to this picture, exciting prospects lie ahead from fixed-target ion-ion collisions at the LHC. The LHCb detector hosts in particular the System for Measuring Overlap with Gas (SMOG2) [29–31], enabling us to perform beam-target collisions at relativistic energy in the centre-of-mass frame ($\sqrt{s_{NN}} = 68.5$ GeV for beam nucleons boosted to 2.5 TeV). This configuration is of unique interest. At $\sqrt{s_{NN}} = 68.5$ GeV, Pb+O or Pb+Ne collisions yield multiplicities close to those of collider-mode proton-nucleus or oxygen-oxygen collisions at LHC energy, and should exhibit visible collective behavior. At the same time, the beam energy is approximately that explored by the BES at RHIC, implying a significantly baryon-rich system. However, the size of the Pb+O and Pb+Ne droplets is somewhat intermediate between the $d+Au$ and $Au+Au$ collisions explored at the BES. Fixed-target collisions at LHC probe, then, a combination of size and baryon density which has not been explored (and will not be explored) by any other experiment.

Characterizations of the matter produced in these experiments have only just begun. The LHCb collaboration has recently published the measurement of J/Ψ and D_0 production in Pb+Ne collisions [30]. The resulting ratio between the two cross sections is consistent with the $p+Ne$ baseline, even in high-multiplicity events, suggesting that hot-medium interactions may not be effective. Experimental studies of the soft sector and the collective flow have not been performed yet. It is crucial to explore if sizable anisotropic flow is observed in these collisions: in the absence of hard-probe modification, this would effectively open a *small system puzzle* in a new type of system. Surprisingly, theoretical studies of anisotropic flow in fixed-target mode are missing. To motivate and underscore the potential of the experimental effort, in this Letter we aim to fill this important gap.

Owing to recent advances in the understanding of the ground-state structure of ^{16}O and ^{20}Ne , as well as of the

longitudinal structure of heavy-ion collisions, we work within an end-to-end hydrodynamic framework based on PGCM/NLEFT+3D-Glauber+MUSIC+UrQMD simulations of Pb+Ne and Pb+O collisions.

The simulations start with configurations of nucleons for ^{20}Ne and ^{16}O obtained from either *ab initio* Projected Generator Coordinate Method (PGCM) [32–34] or Nuclear Lattice Effective Field Theory (NLEFT) [35–37] calculations, as presented in Ref. [38]. The PGCM nucleons are sampled either independently from the intrinsic nuclear densities (labeled hereafter *Independent* configurations) or by enforcing two protons and two neutrons to sit close to α -cluster centers (labeled *Cluster* configurations). For the NLEFT calculation, we do not take into consideration the moderate sign problem that affects the Monte Carlo sampling, and construct expectation values in the final state by assigning a positive weight to each event, which is done by considering only positive-sign nuclear configurations in the hydro calculations (see [38] for a detailed discussion of this matter). This approximation is good enough for the qualitative nature of the present study. For ^{208}Pb , we assume independent nucleons within a matter distribution, $\rho(r)$, corresponding to the measured charge density in Woods-Saxon (W-S) form:

$$\rho(r) \propto (1 + \exp[(r - R)/a])^{-1}, \quad (1)$$

with $R = 6.62$ fm, and $a = 0.55$ fm [39].

Details on the three-dimensional energy- and baryon-density deposition model within the Glauber picture [40] are provided in the Supplemental Material (SM). The MUSIC code [41–43] solves 3+1D relativistic hydrodynamic equations by evolving the initialized densities with lattice QCD based equation of state [44]. When the local energy density drops below 0.45 GeV/fm³, we switch to a hadron gas phase described within the hadron cascade model UrQMD [45, 46]. For each nuclear structure scenario, we run 200k minimum bias events for both Pb+Ne and Pb+O collisions. For each collision event, the particlization to hadrons and the UrQMD evolution are repeated, so that the event is oversampled until we obtain 10^6 hadrons per hydro-surface, irrespective of centrality.

Final state observables are evaluated using all oversampled UrQMD events, which effectively erases *non-flow* contributions and statistical fluctuations. The model parameters used in the calculations are the same as in Ref. [47]. They lead to a good description of the pseudorapidity (η) dependence of the charged yields in $p/d/{}^3He+Au$ collisions at top RHIC energy. The simulations are performed in the centre-of-mass frame, where $\sqrt{s_{NN}} = 68.5$ GeV. The final-state hadrons are then boosted by $\Delta y = y_{\text{beam}}(5.02 \text{ TeV}) - y_{\text{beam}}(68.5 \text{ GeV})$ to the lab frame. The event centrality is determined from the distribution of the charged hadron multiplicity within the acceptance of the LHCb spectrometer, $2 < \eta < 5$, with 0% corresponding to the high-multiplicity limit.

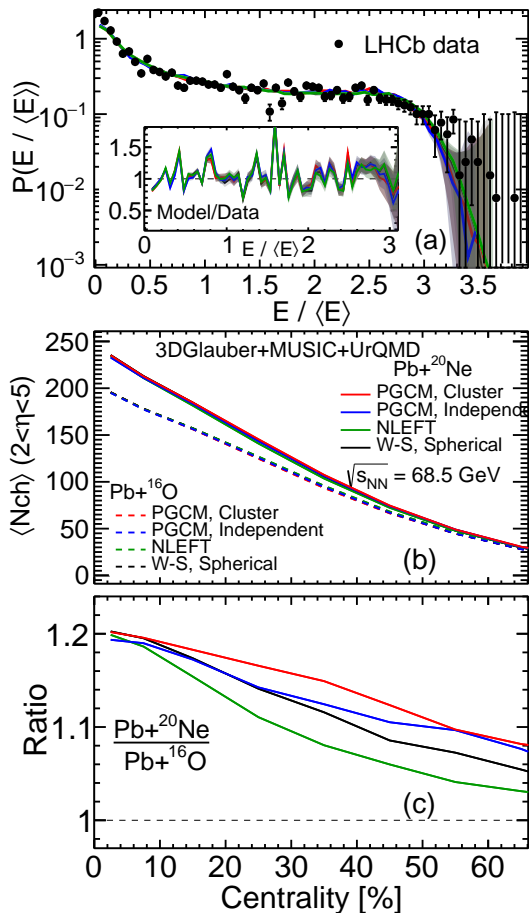


FIG. 1. (a): Probability density of the rescaled energy, $E/\langle E \rangle$, in Pb+Ne and Pb+O collisions at $\sqrt{s_{\text{NN}}} = 68.5$ GeV. Lines are hydrodynamic predictions for different nuclear structure inputs. Symbols are experimental data from the LHCb Collaboration [29]. (b): Hydrodynamic prediction for the charged multiplicity in the LHCb acceptance as a function of the collision centrality. We plot as well the ratio of charged multiplicity taken between Pb+Ne and Pb+O collisions in panel (c). Errors are statistical only and of the same size as the shown lines when not visible.

To start, we calculate the total energy, E , of the final-state hadrons in the lab frame. In Fig. 1(a), the minimum-bias distribution of E , rescaled by the mean value of the full sample, is compared to the histogram of the rescaled energy collected in the electromagnetic calorimeter of LHCb in Pb+Ne collisions [29], which should be strongly correlated with the total event E . Excellent agreement between data and our 3+1D model result is found. We emphasize that agreement is as good as that obtained by the LHCb collaboration via a dedicated Glauber fit of the energy histogram (Fig. 18 in [29]).

Next, we predict the centrality dependence of the average charged multiplicity, $\langle N_{\text{ch}} \rangle$. In Fig. 1(b)-(c), it displays a steeper trend as a function of centrality in Pb+Ne collision than in Pb+O collisions. We understand this

as follows. Due to the larger ^{20}Ne size, Pb+Ne collisions have a higher nucleus-nucleus cross section, which implies larger impact parameters at the same centrality percentile. The size of the ^{208}Pb nucleus is however the same in both systems. Therefore, the number of nucleons that do not hit the incoming ^{208}Pb increases more rapidly with centrality for a ^{20}Ne target than for a ^{16}O target, explaining the steeper trend in Figs. 1(b)-(c).

The qualitative behavior is robust against variations in the nuclear structure input. The NLEFT curve has the steepest decrease because it predicts a larger Ne/O ratio for the nuclear radius than the PGCM calculations [38]. For completeness, we repeat our calculation with spherical ^{20}Ne and ^{16}O nuclei parametrized via Eq. (1) with $R = 2.8$ fm, $a = 0.57$ fm for ^{20}Ne , and $R = 2.61$ fm, $a = 0.51$ fm for ^{16}O [39]. This leads to essentially the same prediction in Fig. 1(c), confirming that the trend is driven by a size effect rather than the ^{20}Ne deformation.

Moving to results involving the anisotropy of the overlap area in Pb+Ne collisions, the novelty and uniqueness of this configuration can be grasped by analyzing the initial-state ellipticity, ε_2 , which sources the final-state elliptic flow. This is quantified via the quadrupole moment of the energy-density field, $\tau e(r, \phi_r)$ [GeV/fm 2], at the beginning of hydrodynamics [48]:

$$\varepsilon_2 = \frac{\left| \int r dr d\phi_r r^2 e^{i2\phi_r} \tau e(r, \phi_r) \right|}{\int r dr d\phi_r r^2 \tau e(r, \phi_r)}, \quad \varepsilon_2\{2\}^2 \equiv \langle \varepsilon_2^2 \rangle, \quad (2)$$

where the average is over events at a given centrality.

Due to the peculiar shape of ^{20}Ne , deformed into a bowling-pin-like $^{16}\text{O} + \alpha$ configuration [38], performing Pb+Ne collisions amounts to playing bowling with the ball (lead) thrown towards the bowling pin (neon) target. When the hit neon lies fully within the area of the lead nucleus, its entire shape is resolved. Naturally, we expect the eccentricity of the overlap region to be nearly constant for those impact parameters that correspond to such a configuration. Given the large size of ^{208}Pb , this explains why the variation of $\varepsilon_2\{2\}$ observed in Fig. 2 in Pb+Ne collisions is so small up to impact parameters of order $b \sim 5$ fm. This behavior seems solid and genuinely induced by the large quadrupole deformation of ^{20}Ne : the calculation for a spherical W-S ^{20}Ne nucleus leads to a steeper (though, predictably, still mild compared to a symmetric, e.g., oxygen-oxygen configuration) centrality dependence for $\varepsilon_2\{2\}$, consistent with the trend of Pb+O collisions for both deformed and spherical ^{16}O nuclei. In terms of observable quantities, we expect thus an enhancement of the elliptic flow of Pb+Ne collisions relative to Pb+O collisions in a broad centrality range.

With this insight in mind we look at the anisotropic flow in momentum space, defined by the set of Fourier harmonics that characterize the azimuthal angle ϕ de-

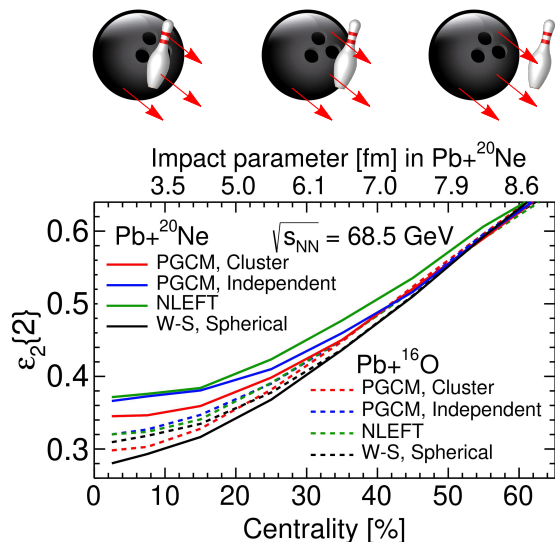


FIG. 2. Playing ultra-relativistic bowling at the LHC. The rms initial-state ellipticity, $\varepsilon_2\{2\}$ is plotted as a function of the centrality percentile in Pb+Ne collisions (solid lines) and Pb+O collisions (dashed lines) at $\sqrt{s_{NN}} = 68.5$ GeV, for various nuclear structure models. Errors are statistical only and of the same size as the line width when not visible. The sketches on top of the figure illustrate the collision geometry based on the average impact parameters of the Pb+Ne collisions (labeling the upper axis of the plot). We recall the ^{208}Pb W-S radius is around 6.6 fm, and about 2.8 fm for ^{20}Ne [39].

pendence of the charged hadron spectrum:

$$\frac{dN_{\text{ch}}}{d\phi} \propto 1 + 2 \sum_{n=1}^{\infty} v_n \cos[n(\phi - \phi_n)], \quad (3)$$

where v_n is the magnitude of the n -th order harmonic. At a given centrality, we evaluate the root mean square value of the distribution of the coefficient (see the SM for further derivations),

$$v_n\{2\} = \sqrt{\langle v_n^2 \rangle}. \quad (4)$$

Figure 3(a) displays our predictions for the elliptic flow ($n = 2$) of Pb+Ne and Pb+O collisions. The centrality dependence of $v_2\{2\}$ in Fig. 3(a) is rather flat, especially when a deformed ^{20}Ne is considered. Computing the Pb+Ne/Pb+O ratio, shown in Fig. 3(b), highlights instead the strong impact of the shape of ^{20}Ne , which enhances the elliptic flow in central Pb+Ne collisions by more than 20%. The signal survives up to large centralities, confirming the intuition from Fig. 2. This showcases the unique power of SMOG2, and in general of asymmetric Pb+X collisions [49], as a tool to image nuclear ground states [50]. For the spherical baseline, the elliptic flow ratio is below unity. This is due to the larger mass number of ^{20}Ne , which reduces initial-state fluctuations with respect to collisions involving ^{16}O nuclei. Indeed, in absence of nuclear deformation corrections, a larger elliptic flow should be observed in Pb+O collisions.

Figures 3(c)-(d) show our predictions for the rms triangular flow, $v_3\{2\}$, in both systems. The predictions seem diametrically opposite to those obtained for the elliptic flow: $v_3\{2\}$ depends strongly on the centrality percentile in Fig. 3(c), while Fig. 3(d) indicates little difference between Pb+Ne and Pb+O systems. This is in agreement with the predictions obtained for the ratio taken between symmetric Ne+Ne and O+O collisions [38].

Moving on to the quadrangular flow ($n = 4$), the same patterns seen in the case of elliptic flow are recovered. In Fig. 3(e), $v_4\{2\}$ shows little variation with centrality, though the ratio of quadrangular flow coefficients in Fig. 3(f) is enhanced by as much as 20% in central Pb+Ne collisions compared to Pb+O. As explicitly demonstrated in the SM, one can identify the origin of such behavior in the non-linear mode coupling between the elliptic and quadrangular flow vectors [51–54]. Therefore, while the shape of ^{20}Ne directly impacts the magnitude of v_2 , it impacts the v_4 indirectly via nonlinear coupling. This extra layer of complexity leads to an even more stringent test of the hydrodynamic model. It should be investigated in experiments, and tested as well within a framework that is not hydrodynamic, such as transport [55].

Before concluding, we analyze a standard probe of hydrodynamic behavior in high-energy collisions, the fourth-order cumulant of the elliptic flow distribution:

$$c_2\{4\} = \langle v_2^4 \rangle - 2\langle v_2^2 \rangle^2, \quad (5)$$

where averages are again over events at a given centrality. As we explain in the SM, this quantity measures the kurtosis of the elliptic flow vector distribution at a given centrality [56, 57], and can have either negative or positive sign. The centrality dependence of $c_2\{4\}$ is shown in Fig. 4(a). Surprisingly, in central collisions we predict:

$$c_2\{4\}_{\text{PbNe}} < 0 < c_2\{4\}_{\text{PbO}}. \quad (6)$$

To get some understanding, we calculate in Fig. 4(b) the same quantity with v_2 in Eq. (5) replaced by the initial-state ellipticity, ε_2 . The sign of the resulting cumulant is negative, and its magnitude is much larger in Pb+Ne collisions than in Pb+O collisions, in agreement with previous studies with deformed nuclei [58, 59]. The hydrodynamic expansion adds a positive correction to the value of $c_2\{4\}$ in a given centrality, changing even the sign of the cumulant in Pb+O collisions, or when a spherical neon is used. Similar results are found for p - p collisions [60, 61]. However, the effect of the ^{20}Ne shape is opposite: the impact of the deformation reduces the kurtosis, causing $c_2\{4\}$ in Pb+Ne collisions to preserve its negative sign after the hydrodynamic evolution. This interplay between the deformation effect and hydrodynamic response provides a nontrivial probe of the dynamics of the collisions, and so we urge the experiments to verify this result.

Note that the parameters of the hydrodynamic model used here do not yet result from a Bayesian analysis of the

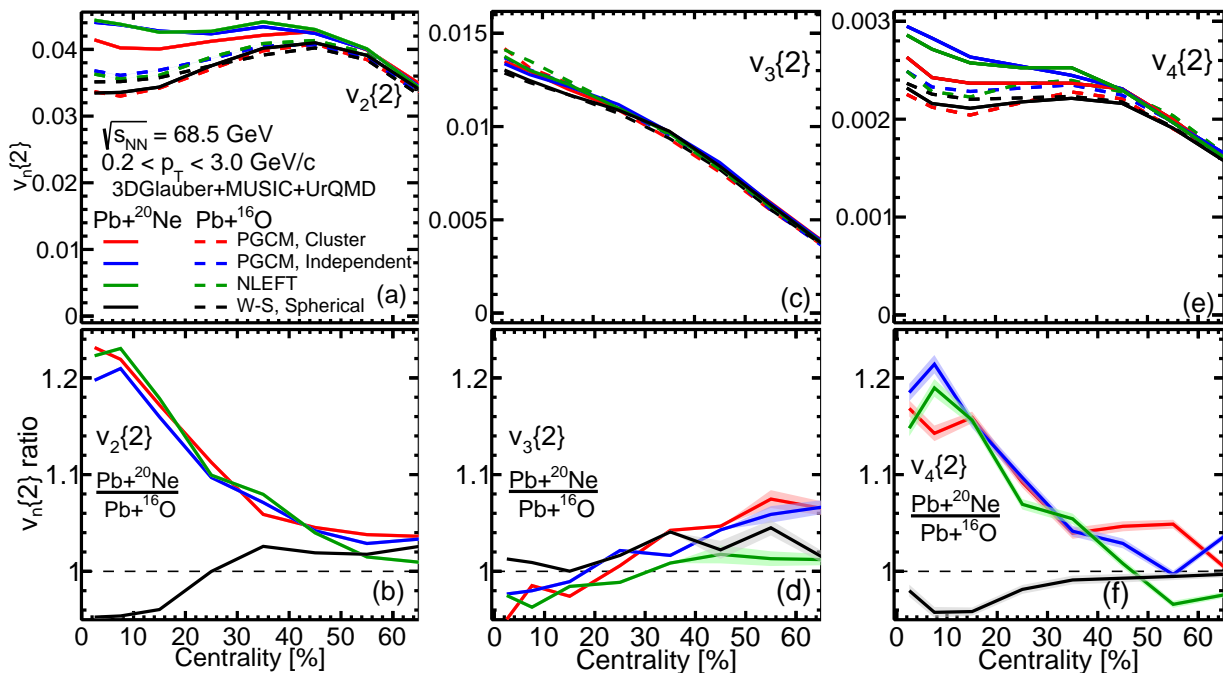


FIG. 3. Anisotropic flow coefficients in Pb+Ne collisions (solid lines) and Pb+O collisions (dashed lines) at $\sqrt{s_{NN}} = 68.5$ GeV, calculated within the LHCb acceptance, as a function of the collision centrality. Upper panels show predictions for the rms elliptic flow, $v_2\{2\}$ (a), triangular flow, $v_3\{2\}$ (c), and quadrangular flow, $v_4\{2\}$ (e). Lower panels show the corresponding ratios taken between Pb+Ne and Pb+O collisions. Different line colors correspond to different nuclear structure inputs. Errors are statistical only and of the same size as the shown lines when not visible.

RHIC BES data. Though unlikely, we can not exclude *a priori* that there may exist a plausible set of parameters (likely, initial-state parameters) for which $c_2^5\{4\}$ has a different sign. In addition, the choice of the variable used to define the collision centrality affects the sign of the cumulant [62, 63]. Systematic analyses to address these points are costly for 3+1D simulations, and outside the scope of present manuscript, but should be carried out for future comparisons with the experimental results.

In summary, we have unveiled the great opportunities offered by studies of the anisotropic flow in fixed-target collisions at the LHCb detector. Our predictions may be amenable to experimental verification already with the next LHC ion run. The availability of the bowling-pin nucleus ^{20}Ne in SMOG2 enables one to isolate strong effects of the hydrodynamic response. If the dramatic enhancements of v_2 and v_4 relative to the Pb+O baseline will be confirmed by the LHCb collaboration, they will hint at the validity of a QGP description. This will pave the way to quantitative characterizations of the matter formed in these experiments via future Bayesian analyses.

The predictions of this manuscript can indeed be improved in several directions. The impact of short-range two-particle correlations (*non flow*) is washed out in our simulations due to the oversampling of the UrQMD events, which can be relaxed in future studies. In addition, a more detailed analysis of the systematics of the

theoretical model will elucidate whether theoretical uncertainties cancel when normalizing Pb+Ne observables with those coming from another collision species [38].

Additional observables can be studied to fully exploit the LHCb data. Focusing on η -differential quantities will help constrain models of longitudinal fluctuations, which are under intense study in the community [64–68]. In addition, probing hydrodynamic behavior via shape-induced modifications of the collective flow can be done as well through the mean transverse momentum, $\langle p_T \rangle$, of final-state hadrons, by measuring its event-by-event fluctuations and the $v_2^2\text{-}\langle p_T \rangle$ correlation [50, 69–80].

Finally, other species are available in SMOG2, notably, nitrogen (N), argon (Ar), krypton (Kr), and xenon (Xe). Their clustered and deformed geometries will have to be elucidated via future *ab initio* computations of nuclear structure based on high-resolution chiral EFT interactions [81, 82], which have only recently been pushed to the description of medium-mass deformed nuclei [83–86]. We are thus looking forward to an exciting program of cross-disciplinary QCD studies centered around the unique high-energy fixed-target mode of the LHC.

The gas-injection system of LHCb has been so far used with a natural neon source. Abundances of stable isotopes in the gas are 90.48% for ^{20}Ne , 0.27% for ^{21}Ne , and 9.25% for ^{22}Ne [87]. We recommend a purified ^{20}Ne sample for use in the experimental campaigns for a trans-

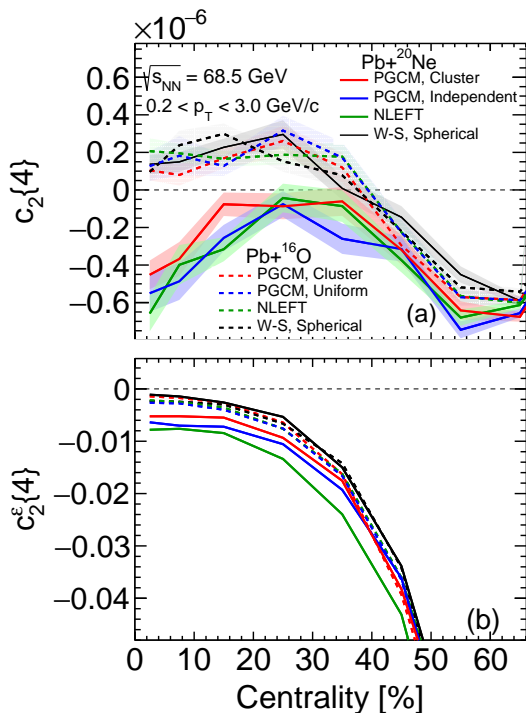


FIG. 4. Centrality dependence of $c_2\{4\}$ computed both from the final-state hadron distributions (upper) and from the initial-state eccentricity distribution (lower) in Pb+Ne collisions (solid lines) and Pb+O collisions (dashed lines) at $\sqrt{s_{NN}} = 68.5$ GeV. Different line colors correspond to different nuclear structure inputs. Errors are statistical only and of the same size as the shown lines when not visible.

parent interpretation of the physics results. This is especially important in the limit of ultra-central collisions with the largest numbers of participant nucleons.

We thank the LHCb Collaboration for sharing with us the data shown in Fig. 1. We thank in particular Giacomo Graziani and the participants of the program+workshop “*Exploring Nuclear Physics Across Energy Scales 2024*” for useful discussions. G.G. is funded by the Deutsche Forschungsgemeinschaft (DFG, German Research Foundation) – Project-ID 273811115 – SFB 1225 ISOQUANT, and under Germany’s Excellence Strategy EXC2181/1-390900948 (the Heidelberg STRUCTURES Excellence Cluster). This material is based upon work supported by the U.S. Department of Energy, Office of Science, Office of Nuclear Physics, under DOE Contract No. DE-SC0012704 (B.P.S.) and Award No. DE-SC0021969 (C.S.), and within the framework of the Saturated Glue (SURGE) Topical Theory Collaboration. C.S. acknowledges a DOE Office of Science Early Career Award. W.B.Z. is supported by DOE under Contract No. DE-AC02-05CH11231, by NSF under Grant No. OAC-2004571 within the X-SCAPE Collaboration, and within the framework of the SURGE Topical Theory Collaboration. This research

was done using resources provided by the Open Science Grid (OSG) [88, 89], which is supported by the National Science Foundation award #2030508. This work is supported in part by the European Research Council (ERC) under the European Union’s Horizon 2020 research and innovation programme (ERC AdG EXOTIC, grant agreement No. 101018170), by DFG and NSFC through funds provided to the Sino-German CRC 110 “Symmetries and the Emergence of Structure in QCD” (NSFC Grant No. 11621131001, DFG Grant No. TRR110). The work of UGM was supported in part by the CAS President’s International Fellowship Initiative (PIFI) (Grant No. 2018DM0034). R.R. is supported by the Deutsche Forschungsgemeinschaft (DFG, German Research Foundation) – Projektnummer 279384907 – SFB 1245. T.R.R. is supported by the Spanish MCIU (PID2021- 127890NB-I00). The PGCM calculations were performed using HPC resources from GENCI-TGCC (Contracts No. A0130513012 and A0150513012) and CCRT (TOPAZE supercomputer). The NLEFT code development and production calculations utilized the following computational resources: the Gauss Centre for Supercomputing e.V. (www.gauss-centre.eu) for computing time on the GCS Supercomputer JUWELS at Jülich Supercomputing Centre (JSC) and special GPU time allocated on JURECA-DC; the Oak Ridge Leadership Computing Facility through the INCITE award “Ab-initio nuclear structure and nuclear reactions”; and the TUBITAK ULAKBIM High Performance and Grid Computing Center (TRUBA resources). J.N.H. acknowledges financial support from the US-DOE Nuclear Science Grant No. DE-SC0023861 and within the framework of the Saturated Glue (SURGE) Topical Theory.

SUPPLEMENTAL MATERIAL

3D Glauber Monte Carlo initial conditions

The 3D Monte-Carlo Glauber model is a dynamical event-by-event initial condition [40, 90], that provides the space-time and momentum distributions of the initial energy-momentum tensor and net baryon charge current, employing a classical string deceleration model [90, 91]. The transverse positions of valence quarks and the soft partonic cloud in wounded nucleons are sampled from a 2D Gaussian. After the collision, the deposited energy density distribution and baryon charge have Gaussian profiles in the transverse plane. The average rapidity loss function of the valence quarks and the soft partonic cloud with their incoming rapidity y_{init} in the collision pair rest frame is parameterized as [40, 92],

$$\langle y_{\text{loss}} \rangle (y_{\text{init}}) = A y_{\text{init}}^{\alpha_2} [\tanh(y_{\text{init}})]^{\alpha_1 - \alpha_2}. \quad (7)$$

The parameters are fixed by fitting the measured

pseudo-rapidity distributions of charged hadrons for Au+Au and light-ion collisions [12, 40, 47, 92]. The detailed implementation of this initial condition model is discussed in Ref. [40]. The pre-hydrodynamic flow is included by a finite transverse initial velocity [47]. Finally, the produced strings from individual nucleon-nucleon collisions are treated as dynamical source terms for the hydrodynamic evolution [40, 90, 93, 94].

CUMULANTS OF FLOW FLUCTUATIONS IN THE LAB FRAME

We recall here the definition and the physical meaning of the cumulants of anisotropic flow fluctuations, $v_n\{2\}$ and $c_2\{4\}$, analyzed in this manuscript.

We start with the harmonic decomposition of the measured charged-hadron spectrum,

$$\frac{dN}{d\phi_p} = \sum_{n=-\infty}^{+\infty} \mathbf{v}_n e^{in\phi_p}, \quad \mathbf{v}_{-n} = \mathbf{v}_n^*, \quad (8)$$

where ϕ_p is the azimuthal angle of transverse momentum and the set of complex coefficients \mathbf{v}_n define the anisotropic flow. Note that \mathbf{v}_n comes with a real and an imaginary part

$$\mathbf{v}_n = (v_x, v_y) \quad (9)$$

which depends on the choice of the coordinate frame. Typically, x and y label either the transverse plane in the laboratory frame or the frame of the reaction plane with x chosen along the impact parameter direction.

Observables constructed from the anisotropic flow in heavy-ion collisions are measured as statistical averages involving azimuthal angles, which are taken over collision events, typically at a fixed final-state multiplicity (centrality). In the sample of events, the flow vector, \mathbf{v}_n , has some underlying distribution:

$$P(\mathbf{v}_n) = P(v_x, v_y), \quad v_n = \sqrt{v_x^2 + v_y^2}. \quad (10)$$

Experimentally, the aim is to characterize such probability distribution in a given centrality class, which yields detailed information about the evolution and the properties of the produced matter.

Cumulants fully characterize a probability distribution and are particularly useful in this context. The cumulant generating function of the distribution of \mathbf{v}_n is defined by:

$$\ln G(\mathbf{k}) = \ln \int d\mathbf{v}_n P(\mathbf{v}_n) e^{\mathbf{k} \cdot \mathbf{v}_n} = \ln \langle e^{\mathbf{k} \cdot \mathbf{v}_n} \rangle, \quad (11)$$

from which the cumulant of order m is derived as $\partial_{\mathbf{k}}^{(m)} \ln G(\mathbf{k})|_{\mathbf{k}=0}$. In nuclear collisions, while the magnitude of the impact parameter can be controlled from the number of final-state particles, its orientation is always random. Therefore, experiments only access the

angle-averaged information about the \mathbf{v}_n harmonics, i.e., moments of the magnitude, v_n , but can not reconstruct information about the individual $v_{x,y}$ components. In practice, we write the vector $\mathbf{k} = (k \cos \varphi, k \sin \varphi)$, and we are forced to average over the angle in Eq. (11), which yields:

$$\ln G(k) = \ln \left\langle \int_0^{2\pi} \frac{d\varphi}{2\pi} e^{\mathbf{k} \cdot \mathbf{v}_n} \right\rangle = \ln \langle I_0(kv_n) \rangle. \quad (12)$$

Information is lost and we end up with a modified Bessel function, I_0 , which is an even function. The cumulants of the angle-averaged distribution of the \mathbf{v}_n vector, whose standard notation is $v_n\{m\}^m$, are then obtained from the equality:

$$\ln \langle I_0(kv_n) \rangle = \sum_{m=0}^{\infty} c_m k^m v_n\{m\}^m. \quad (13)$$

The integer $m \geq 2$ is an even number, while the coefficients c_m have to be matched to the power expansion of the left-hand side, that is:

$$\ln \langle I_0(kv_n) \rangle = \ln \left(1 + \frac{\langle v_n^2 \rangle k^2}{4} - \frac{\langle v_n^4 \rangle k^4}{64} + \frac{\langle v_n^6 \rangle k^6}{576} + \dots \right). \quad (14)$$

Expanding this logarithm in powers of k , and matching to the right-hand side of Eq. (13), one obtains:

$$\begin{aligned} v_n\{2\}^2 &= \langle v_n^2 \rangle, \\ v_n\{4\}^4 &= 2\langle v_n^2 \rangle^2 - \langle v_n^4 \rangle, \\ v_n\{6\}^6 &= \frac{1}{4} (\langle v_n^6 \rangle - 9\langle v_n^4 \rangle \langle v_n^2 \rangle + 12\langle v_n^2 \rangle^3), \end{aligned} \quad (15)$$

and so on, where averages are over events at a given centrality. The cumulants are thus expressed in terms of even moments of the distribution of v_n , of the form $\langle v_n^{2k} \rangle$. These moments represent the quantities that can be measured in the experiments from established multiparticle correlation techniques [2].

As pointed out in Ref. [95], it is insightful to relate the observable quantities on the left-hand side of Eq. (15) to an expansion involving the (non-measurable) cumulants of the individual x and y components of \mathbf{v}_n . Up to fourth order, the cumulants of the projections are:

$$\begin{aligned} \kappa_{10} &= \langle v_x \rangle, & \kappa_{01} &= \langle v_y \rangle, \\ \kappa_{20} &= \langle (v_x - \kappa_{10})^2 \rangle, & \kappa_{02} &= \langle (v_y - \kappa_{01})^2 \rangle, \\ \kappa_{30} &= \langle (v_x - \kappa_{10})^3 \rangle, & \kappa_{03} &= \langle (v_y - \kappa_{01})^3 \rangle, \\ \kappa_{12} &= \langle (v_x - \kappa_{10})(v_y - \kappa_{01})^2 \rangle, \\ \kappa_{21} &= \langle (v_x - \kappa_{10})^2(v_y - \kappa_{01}) \rangle, \\ \kappa_{40} &= \langle (v_x - \kappa_{10})^4 \rangle - 3\kappa_{20}^2, \\ \kappa_{04} &= \langle (v_y - \kappa_{01})^4 \rangle - 3\kappa_{02}^2, \\ \kappa_{22} &= \langle (v_x - \kappa_{10})^2(v_y - \kappa_{01})^2 \rangle - \kappa_{20}\kappa_{02}. \end{aligned} \quad (16)$$

If x and y parametrize the transverse plane in the lab frame, the odd moments of the v_x and v_y distributions vanish (for an ideal detector), meaning that we are only left with non-zero values for κ_{20} , κ_{02} , κ_{40} , κ_{04} , κ_{22} . A little algebra [56, 57, 95] shows that the first two cumulants in Eq. (15) can consequently be written as:

$$v_n\{2\}^2 = \kappa_{20} + \kappa_{02}, \quad (17)$$

$$v_n\{4\}^4 = -(\kappa_{04} + \kappa_{40} + 2\kappa_{22}). \quad (18)$$

This implies the following. The second-order cumulant $v_2\{2\}^2$ isolates the variance of the two-dimensional distribution. It tells us how a change in the mean square value of the flow vector magnitude, $\langle v_n^2 \rangle$, is associated with an increase in the variances of its x and y components. Concerning the fourth-order cumulant, conventionally denoted by ¹

$$c_2\{4\} \equiv -v_2\{4\}^4, \quad (19)$$

it isolates instead the kurtosis correction, and vanishes if $P(v_x, v_y)$ is a two-dimensional Gaussian.

We understand then the impact of the shape of ^{20}Ne on the elliptic flow vector, \mathbf{v}_2 :

- The increase of $v_2\{2\}$ induced by the deformation of the nucleus is due to an isotropic increase in spread of the two-dimensional \mathbf{v}_2 distribution (see also [96]).
- The increase in $c_2\{4\}$ implies instead that larger elliptic flow fluctuations lead as well to enhanced non-Gaussian tails. The kurtosis comes with a positive sign in the expression of $c_2\{4\}$, therefore, nuclear deformation reduces the kurtosis leading to a platykurtic distribution (tails thinner than a Gaussian) at a given centrality.

UNDERSTANDING THE ENHANCEMENT OF v_4

Here we explain the enhancement of $v_4\{2\}$ in central Pb+Ne collisions relative to central Pb+O collisions observed in Fig. 3. We recall that the quadrangular flow vector, $\mathbf{v}_4 = v_4 e^{i4\phi_4}$, can by virtue of symmetry be decomposed as follows [53],

$$\mathbf{v}_4 = \mathbf{v}_{4L} + \chi_4 \mathbf{v}_2^2, \quad (20)$$

where χ_4 is a coefficient that quantifies the strength of the nonlinear coupling to the squared elliptic flow vector,

$\mathbf{v}_2 = v_2 e^{i2\phi_2}$, while \mathbf{v}_{4L} is defined as the vector statistically uncorrelated with \mathbf{v}_2 in the considered centrality class, that is,

$$\langle \mathbf{v}_{4L} \mathbf{v}_2^{2*} \rangle = 0. \quad (21)$$

With these definitions, one obtains that the mean squared quadrangular flow is the sum of two contributions that add in quadrature,

$$\langle v_4^2 \rangle = \langle v_{4L}^2 \rangle + \chi_4^2 \langle v_2^4 \rangle, \quad (22)$$

where $v_4 = |\mathbf{v}_4|$, $v_2 = |\mathbf{v}_2|$, $v_{4L} = |\mathbf{v}_{4L}|$.

Now we take the ratio between Pb+Ne and Pb+O collisions, i.e.,

$$\frac{\langle v_4^2 \rangle_{\text{PbNe}}}{\langle v_4^2 \rangle_{\text{PbO}}} = \frac{\langle v_{4L}^2 \rangle_{\text{PbNe}} + \chi_{4,\text{PbNe}}^2 \langle v_2^4 \rangle_{\text{PbNe}}}{\langle v_{4L}^2 \rangle_{\text{PbO}} + \chi_{4,\text{PbO}}^2 \langle v_2^4 \rangle_{\text{PbO}}}. \quad (23)$$

In central collisions, one expects the term coupling to elliptic flow to be sub-leading compared to the uncorrelated contribution, $\langle v_{4L}^2 \rangle \gg \chi_4 \langle v_2^4 \rangle$. This justifies a Taylor expansion of the previous expression:

$$\begin{aligned} \frac{\langle v_4^2 \rangle_{\text{PbNe}}}{\langle v_4^2 \rangle_{\text{PbO}}} &= \\ &= \frac{\langle v_{4L}^2 \rangle_{\text{PbNe}}}{\langle v_{4L}^2 \rangle_{\text{PbO}}} + \frac{\chi_{4,\text{PbNe}}^2 \langle v_2^4 \rangle_{\text{PbNe}}}{\langle v_{4L}^2 \rangle_{\text{PbO}}} - \frac{\langle v_{4L}^2 \rangle_{\text{PbNe}}}{(\langle v_{4L}^2 \rangle_{\text{PbO}})^2} \chi_{4,\text{PbO}}^2 \langle v_2^4 \rangle_{\text{PbO}}. \end{aligned} \quad (24)$$

Now, we show in Fig. 5 hydrodynamic results for $\chi_{4,22}$ [panel (a)] and $\langle v_{4L}\{2\} \equiv \sqrt{\langle v_{4L}^2 \rangle}$ [panel (b)]. We see that both these quantities are rather universal and receive only percent-level corrections if one varies the nuclear species/structure. For simplicity, let us then consider that

$$\langle v_{4L}^2 \rangle_{\text{PbNe}} = \langle v_{4L}^2 \rangle_{\text{PbO}} \equiv \langle v_{4L}^2 \rangle, \quad (25)$$

$$\chi_{4,\text{PbNe}} = \chi_{4,\text{PbO}} \equiv \chi_4. \quad (26)$$

With this, we can rewrite Eq. (24) as follows:

$$\frac{v_4^2\{2\}_{\text{PbNe}}}{v_4^2\{2\}_{\text{PbO}}} \equiv \frac{\langle v_4^2 \rangle_{\text{PbNe}}}{\langle v_4^2 \rangle_{\text{PbO}}} = 1 + \chi_4^2 \frac{\langle v_2^4 \rangle_{\text{PbNe}}}{\langle v_{4L}^2 \rangle} \left(1 - \frac{\langle v_2^4 \rangle_{\text{PbO}}}{\langle v_4^2 \rangle_{\text{PbNe}}} \right). \quad (27)$$

This equality should hold in central collisions if the departure from unity in the quadrangular flow ratio is due to the nonlinear coupling term to the elliptic flow. Plugging in numbers from the 0-5% class, we obtain the results shown in Fig. 5(c). Agreement between the $v_4\{2\}$ ratio and the prediction of Eq. (27) is excellent in central collisions, confirming that it is the nonlinear coupling to elliptic flow that drives the nontrivial Pb+Ne to Pb+O ratio.

¹ The sign takes into account the negative sign of the k^4 term in the expansion of Eq. (14).

* gialalone@thphys.uni-heidelberg.de

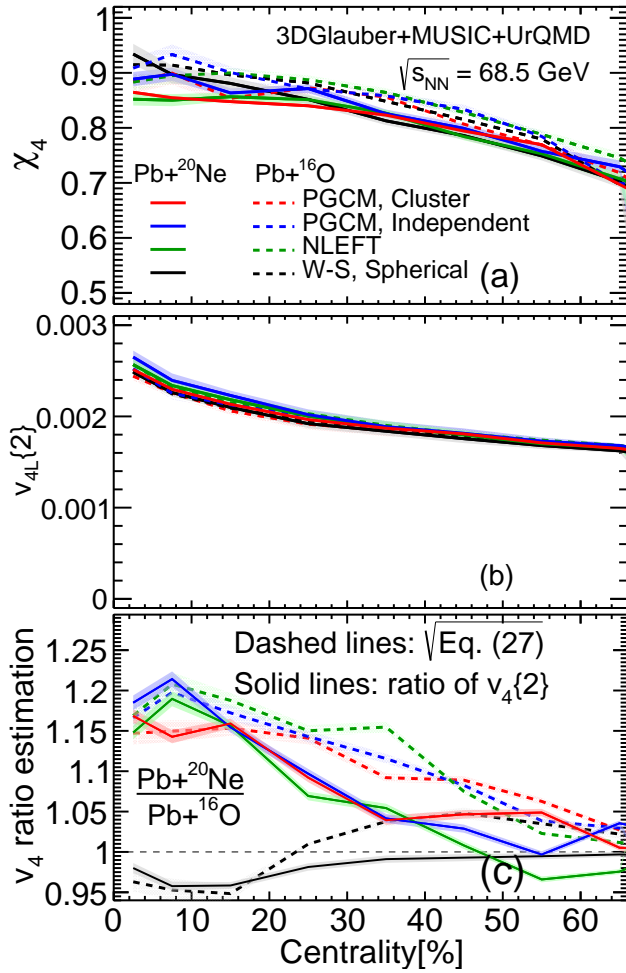


FIG. 5. Centrality dependence of the non-linear coupling coefficient χ_4 (a), of the linear flow mode $v_{4L}\{2\}$ (b), and of the v_4 ratio (c) in Pb+Ne and Pb+O collisions at $\sqrt{s_{NN}} = 68.5$ GeV. The dashed line in panel (c) corresponds to the estimate of Eq. (27). Errors are statistical only and of the same size as the shown lines when not visible.

[†] WenbinZhao@lbl.gov

[‡] bschenke@bnl.gov

[§] chunshen@wayne.edu

- [1] J. W. Harris and B. Müller, “QGP Signatures” revisited, *Eur. Phys. J. C* **84** (2024) no. 3 247.
- [2] J.-Y. Ollitrault, Measures of azimuthal anisotropy in high-energy collisions, *Eur. Phys. J. A* **59** (2023) no. 10 236 [arXiv:2308.11674 [nucl-ex]].
- [3] L. Apolinário, Y.-J. Lee and M. Winn, Heavy quarks and jets as probes of the QGP, *Prog. Part. Nucl. Phys.* **127** (2022) 103990 [arXiv:2203.16352 [hep-ph]].
- [4] J. L. Nagle and W. A. Zajc, Small System Collectivity in Relativistic Hadronic and Nuclear Collisions, *Ann. Rev. Nucl. Part. Sci.* **68** (2018) 211 [arXiv:1801.03477 [nucl-ex]].
- [5] C. Shen and L. Yan, Recent development of hydrodynamic modeling in heavy-ion collisions, *Nucl. Sci. Tech.* **31** (10, 2020) 122 [arXiv:2010.12377 [nucl-th]].
- [6] B. Schenke, The smallest fluid on Earth, *Rept. Prog.*

Phys. **84** (2021) no. 8 082301 [arXiv:2102.11189 [nucl-th]].

- [7] J. Noronha, B. Schenke, C. Shen and W. Zhao 1, 2024, arXiv:2401.09208 [nucl-th].
- [8] CMS collaboration, V. Khachatryan et al., Evidence for collectivity in pp collisions at the LHC, *Phys. Lett. B* **765** (2017) 193 [arXiv:1606.06198 [nucl-ex]].
- [9] ATLAS collaboration, M. Aaboud et al., Correlated long-range mixed-harmonic fluctuations measured in pp, p+Pb and low-multiplicity Pb+Pb collisions with the ATLAS detector, *Phys. Lett. B* **789** (2019) 444 [arXiv:1807.02012 [nucl-ex]].
- [10] ALICE collaboration, S. Acharya et al., Investigations of Anisotropic Flow Using Multiparticle Azimuthal Correlations in pp, p-Pb, Xe-Xe, and Pb-Pb Collisions at the LHC, *Phys. Rev. Lett.* **123** (2019) no. 14 142301 [arXiv:1903.01790 [nucl-ex]].
- [11] ATLAS collaboration, G. Aad et al., Two-particle azimuthal correlations in photonuclear ultraperipheral Pb+Pb collisions at 5.02 TeV with ATLAS, *Phys. Rev. C* **104** (2021) no. 1 014903 [arXiv:2101.10771 [nucl-ex]].
- [12] W. Zhao, C. Shen and B. Schenke, Collectivity in Ultraperipheral Pb+Pb Collisions at the Large Hadron Collider, *Phys. Rev. Lett.* **129** (2022) no. 25 252302 [arXiv:2203.06094 [nucl-th]].
- [13] Y.-C. Chen et al., Long-range near-side correlation in e^+e^- Collisions at 183-209 GeV with ALEPH Archived Data, arXiv:2312.05084 [hep-ex].
- [14] ATLAS collaboration, G. Aad et al., Measurement of long-range pseudorapidity correlations and azimuthal harmonics in $\sqrt{s_{NN}} = 5.02$ TeV proton-lead collisions with the ATLAS detector, *Phys. Rev. C* **90** (2014) no. 4 044906 [arXiv:1409.1792 [hep-ex]].
- [15] ALICE collaboration, J. Adam et al., Multiplicity dependence of charged pion, kaon, and (anti)proton production at large transverse momentum in p-Pb collisions at $\sqrt{s_{NN}} = 5.02$ TeV, *Phys. Lett. B* **760** (2016) 720 [arXiv:1601.03658 [nucl-ex]].
- [16] J. Berges, M. P. Heller, A. Mazeliauskas and R. Venugopalan, QCD thermalization: Ab initio approaches and interdisciplinary connections, *Rev. Mod. Phys.* **93** (2021) no. 3 035003 [arXiv:2005.12299 [hep-th]].
- [17] A. Soloviev, Hydrodynamic attractors in heavy ion collisions: a review, *Eur. Phys. J. C* **82** (2022) no. 4 319 [arXiv:2109.15081 [hep-th]].
- [18] PHOBOS collaboration, B. Alver et al., System size, energy, pseudorapidity, and centrality dependence of elliptic flow, *Phys. Rev. Lett.* **98** (2007) 242302 [arXiv:nucl-ex/0610037].
- [19] STAR collaboration, L. Adamczyk et al., Beam Energy Dependence of the Third Harmonic of Azimuthal Correlations in Au+Au Collisions at RHIC, *Phys. Rev. Lett.* **116** (2016) no. 11 112302 [arXiv:1601.01999 [nucl-ex]].
- [20] STAR collaboration, L. Adamczyk et al., Harmonic decomposition of three-particle azimuthal correlations at energies available at the BNL Relativistic Heavy Ion Collider, *Phys. Rev. C* **98** (2018) no. 3 034918 [arXiv:1701.06496 [nucl-ex]].
- [21] HADES collaboration, J. Adamczewski-Musch et al., Probing dense baryon-rich matter with virtual photons, *Nature Phys.* **15** (2019) no. 10 1040.

- [22] **STAR** collaboration, M. S. Abdallah *et. al.*, *Disappearance of partonic collectivity in $s_{NN}=3\text{GeV}$ Au+Au collisions at RHIC*, *Phys. Lett. B* **827** (2022) 137003 [[arXiv:2108.00908](#) [[nucl-ex](#)]].
- [23] **HADES** collaboration, J. Adamczewski-Musch *et. al.*, *Proton, deuteron and triton flow measurements in Au+Au collisions at $\sqrt{s_{NN}} = 2.4\text{ GeV}$* , *Eur. Phys. J. A* **59** (2023) no. 4 80 [[arXiv:2208.02740](#) [[nucl-ex](#)]].
- [24] E. Annala, T. Gorda, A. Kurkela, J. Nättilä and A. Vuorinen, *Evidence for quark-matter cores in massive neutron stars*, *Nature Phys.* **16** (2020) no. 9 907 [[arXiv:1903.09121](#) [[astro-ph.HE](#)]].
- [25] M. Omana Kuttan, J. Steinheimer, K. Zhou and H. Stoecker, *QCD Equation of State of Dense Nuclear Matter from a Bayesian Analysis of Heavy-Ion Collision Data*, *Phys. Rev. Lett.* **131** (2023) no. 20 202303 [[arXiv:2211.11670](#) [[hep-ph](#)]].
- [26] G. Giacalone, G. Nijs and W. van der Schee, *Determination of the Neutron Skin of Pb208 from Ultrarelativistic Nuclear Collisions*, *Phys. Rev. Lett.* **131** (2023) no. 20 202302 [[arXiv:2305.00015](#) [[nucl-th](#)]].
- [27] J.-F. Paquet, *Applications of emulation and Bayesian methods in heavy-ion physics*, [arXiv:2310.17618](#) [[nucl-th](#)].
- [28] C. Shen, B. Schenke and W. Zhao, *Viscosities of the Baryon-Rich Quark-Gluon Plasma from Beam Energy Scan Data*, *Phys. Rev. Lett.* **132** (2024) no. 7 072301 [[arXiv:2310.10787](#) [[nucl-th](#)]].
- [29] **LHCb** collaboration, R. Aaij *et. al.*, *Centrality determination in heavy-ion collisions with the LHCb detector*, *JINST* **17** (2022) no. 05 P05009 [[arXiv:2111.01607](#) [[nucl-ex](#)]].
- [30] **LHCb** collaboration, R. Aaij *et. al.*, *J/ψ and D^0 production in $\sqrt{s_{NN}} = 68.5\text{ GeV}$ PbNe collisions*, *Eur. Phys. J. C* **83** (2023) no. 7 658 [[arXiv:2211.11652](#) [[hep-ex](#)]].
- [31] S. Mariani, *LHCb Fixed-target results and prospects*, *PoS EPS-HEP2021* (2022) 396.
- [32] M. Frosini, T. Duguet, J.-P. Ebran and V. Somà, *Multi-reference many-body perturbation theory for nuclei: I. Novel PGCM-PT formalism*, *Eur. Phys. J. A* **58** (2022) no. 4 62 [[arXiv:2110.15737](#) [[nucl-th](#)]].
- [33] M. Frosini, T. Duguet, J.-P. Ebran, B. Bally, T. Mongelli, T. R. Rodríguez, R. Roth and V. Somà, *Multi-reference many-body perturbation theory for nuclei: II. Ab initio study of neon isotopes via PGCM and IM-NCSM calculations*, *Eur. Phys. J. A* **58** (2022) no. 4 63 [[arXiv:2111.00797](#) [[nucl-th](#)]].
- [34] M. Frosini, T. Duguet, J.-P. Ebran, B. Bally, H. Hergert, T. R. Rodríguez, R. Roth, J. Yao and V. Somà, *Multi-reference many-body perturbation theory for nuclei: III. Ab initio calculations at second order in PGCM-PT*, *Eur. Phys. J. A* **58** (2022) no. 4 64 [[arXiv:2111.01461](#) [[nucl-th](#)]].
- [35] D. Lee, *Lattice simulations for few- and many-body systems*, *Prog. Part. Nucl. Phys.* **63** (2009) 117 [[arXiv:0804.3501](#) [[nucl-th](#)]].
- [36] T. A. Lähde and U.-G. Meißner, *Nuclear Lattice Effective Field Theory: An introduction*, vol. 957. Springer, 2019.
- [37] D. Lee, *Recent Progress in Nuclear Lattice Simulations*, *Front. in Phys.* **8** (2020) 174.
- [38] G. Giacalone *et. al.*, *The unexpected uses of a bowling pin: exploiting ^{20}Ne isotopes for precision characterizations of collectivity in small systems*, [arXiv:2402.05995](#) [[nucl-th](#)].
- [39] H. De Vries, C. W. De Jager and C. De Vries, *Nuclear charge and magnetization density distribution parameters from elastic electron scattering*, *Atom. Data Nucl. Data Tabl.* **36** (1987) 495.
- [40] C. Shen and B. Schenke, *Longitudinal dynamics and particle production in relativistic nuclear collisions*, *Phys. Rev. C* **105** (2022) no. 6 064905 [[arXiv:2203.04685](#) [[nucl-th](#)]].
- [41] B. Schenke, S. Jeon and C. Gale, *(3+1)D hydrodynamic simulation of relativistic heavy-ion collisions*, *Phys. Rev. C* **82** (2010) 014903 [[arXiv:1004.1408](#) [[hep-ph](#)]].
- [42] J.-F. Paquet, C. Shen, G. S. Denicol, M. Luzum, B. Schenke, S. Jeon and C. Gale, *Production of photons in relativistic heavy-ion collisions*, *Phys. Rev. C* **93** (2016) no. 4 044906 [[arXiv:1509.06738](#) [[hep-ph](#)]].
- [43] G. S. Denicol, C. Gale, S. Jeon, A. Monnai, B. Schenke and C. Shen, *Net baryon diffusion in fluid dynamic simulations of relativistic heavy-ion collisions*, *Phys. Rev. C* **98** (2018) no. 3 034916 [[arXiv:1804.10557](#) [[nucl-th](#)]].
- [44] A. Monnai, B. Schenke and C. Shen, *Equation of state at finite densities for QCD matter in nuclear collisions*, *Phys. Rev. C* **100** (2019) no. 2 024907 [[arXiv:1902.05095](#) [[nucl-th](#)]].
- [45] S. A. Bass *et. al.*, *Microscopic models for ultrarelativistic heavy ion collisions*, *Prog. Part. Nucl. Phys.* **41** (1998) 255 [[arXiv:nucl-th/9803035](#)].
- [46] M. Bleicher *et. al.*, *Relativistic hadron hadron collisions in the ultrarelativistic quantum molecular dynamics model*, *J. Phys. G* **25** (1999) 1859 [[arXiv:hep-ph/9909407](#)].
- [47] W. Zhao, S. Ryu, C. Shen and B. Schenke, *3D structure of anisotropic flow in small collision systems at energies available at the BNL Relativistic Heavy Ion Collider*, *Phys. Rev. C* **107** (2023) no. 1 014904 [[arXiv:2211.16376](#) [[nucl-th](#)]].
- [48] D. Teaney and L. Yan, *Triangularity and Dipole Asymmetry in Heavy Ion Collisions*, *Phys. Rev. C* **83** (2011) 064904 [[arXiv:1010.1876](#) [[nucl-th](#)]].
- [49] B. Bally *et. al.*, *Imaging the initial condition of heavy-ion collisions and nuclear structure across the nuclide chart*, [arXiv:2209.11042](#) [[nucl-ex](#)].
- [50] **STAR** collaboration, *Imaging Shapes of Atomic Nuclei in High-Energy Nuclear Collisions*, [arXiv:2401.06625](#) [[nucl-ex](#)].
- [51] F. G. Gardim, F. Grassi, M. Luzum and J.-Y. Ollitrault, *Mapping the hydrodynamic response to the initial geometry in heavy-ion collisions*, *Phys. Rev. C* **85** (2012) 024908 [[arXiv:1111.6538](#) [[nucl-th](#)]].
- [52] D. Teaney and L. Yan, *Non linearities in the harmonic spectrum of heavy ion collisions with ideal and viscous hydrodynamics*, *Phys. Rev. C* **86** (2012) 044908 [[arXiv:1206.1905](#) [[nucl-th](#)]].
- [53] L. Yan and J.-Y. Ollitrault, $\nu_4, \nu_5, \nu_6, \nu_7$: *nonlinear hydrodynamic response versus LHC data*, *Phys. Lett. B* **744** (2015) 82 [[arXiv:1502.02502](#) [[nucl-th](#)]].
- [54] J. Qian, U. W. Heinz and J. Liu, *Mode-coupling effects in anisotropic flow in heavy-ion collisions*, *Phys. Rev. C* **93** (2016) no. 6 064901 [[arXiv:1602.02813](#) [[nucl-th](#)]].
- [55] J. Jia, G. Giacalone and C. Zhang, *Precision Tests of the Nonlinear Mode Coupling of Anisotropic Flow via High-Energy Collisions of Isobars*, *Chin. Phys. Lett.* **40**

- (2023) no. 4 042501 [arXiv:2206.07184 [nucl-th]].
- [56] N. Abbasi, D. Allahbakhshi, A. Davody and S. F. Taghavi, *Standardized Cumulants of Flow Harmonic Fluctuations*, *Phys. Rev. C* **98** (2018) no. 2 024906 [arXiv:1704.06295 [nucl-th]].
- [57] R. S. Bhalerao, G. Giacalone and J.-Y. Ollitrault, *Kurtosis of elliptic flow fluctuations*, *Phys. Rev. C* **99** (2019) no. 1 014907 [arXiv:1811.00837 [nucl-th]].
- [58] G. Giacalone, *Elliptic flow fluctuations in central collisions of spherical and deformed nuclei*, *Phys. Rev. C* **99** (2019) no. 2 024910 [arXiv:1811.03959 [nucl-th]].
- [59] H. Mehrabpour and S. M. A. Tabatabaee, *Flow distribution analysis as a probe of nuclear deformation*, *Phys. Rev. C* **108** (2023) no. 3 034902 [arXiv:2301.07770 [nucl-th]].
- [60] W. Zhao, Y. Zhou, H. Xu, W. Deng and H. Song, *Hydrodynamic collectivity in proton–proton collisions at 13 TeV*, *Phys. Lett. B* **780** (2018) 495 [arXiv:1801.00271 [nucl-th]].
- [61] W. Zhao, Y. Zhou, K. Murase and H. Song, *Searching for small droplets of hydrodynamic fluid in proton–proton collisions at the LHC*, *Eur. Phys. J. C* **80** (2020) no. 9 846 [arXiv:2001.06742 [nucl-th]].
- [62] M. Zhou and J. Jia, *Centrality fluctuations in heavy-ion collisions*, *Phys. Rev. C* **98** (2018) no. 4 044903 [arXiv:1803.01812 [nucl-th]].
- [63] ATLAS collaboration, M. Aaboud *et al.*, *Fluctuations of anisotropic flow in Pb+Pb collisions at $\sqrt{s_{NN}} = 5.02$ TeV with the ATLAS detector*, *JHEP* **01** (2020) 051 [arXiv:1904.04808 [nucl-ex]].
- [64] D. Soeder, W. Ke, J. F. Paquet and S. A. Bass, *Bayesian parameter estimation with a new three-dimensional initial-conditions model for ultrarelativistic heavy-ion collisions*, arXiv:2306.08665 [nucl-th].
- [65] S. McDonald, S. Jeon and C. Gale, *3+1D initialization and evolution of the glasma*, *Phys. Rev. C* **108** (2023) no. 6 064910 [arXiv:2306.04896 [hep-ph]].
- [66] O. Garcia-Montero, H. Elfner and S. Schlichting, *McDIPPER: A novel saturation-based 3+1D initial-state model for heavy ion collisions*, *Phys. Rev. C* **109** (2024) no. 4 044916 [arXiv:2308.11713 [hep-ph]].
- [67] A. Ipp, M. Leuthner, D. I. Müller, S. Schlichting, K. Schmidt and P. Singh, *Energy-momentum tensor of the dilute (3+1)D Glasma*, arXiv:2401.10320 [hep-ph].
- [68] C. Zhang, S. Huang and J. Jia, *Longitudinal Structure of Quark-Gluon Plasma Unveiled Through Nuclear Deformations*, arXiv:2405.08749 [nucl-th].
- [69] G. Giacalone, *Observing the deformation of nuclei with relativistic nuclear collisions*, *Phys. Rev. Lett.* **124** (2020) no. 20 202301 [arXiv:1910.04673 [nucl-th]].
- [70] G. Giacalone, *Constraining the quadrupole deformation of atomic nuclei with relativistic nuclear collisions*, *Phys. Rev. C* **102** (2020) no. 2 024901 [arXiv:2004.14463 [nucl-th]].
- [71] J. Jia, S. Huang and C. Zhang, *Probing nuclear quadrupole deformation from correlation of elliptic flow and transverse momentum in heavy ion collisions*, *Phys. Rev. C* **105** (2022) no. 1 014906 [arXiv:2105.05713 [nucl-th]].
- [72] J. Jia, *Shape of atomic nuclei in heavy ion collisions*, *Phys. Rev. C* **105** (2022) no. 1 014905 [arXiv:2106.08768 [nucl-th]].
- [73] B. Bally, M. Bender, G. Giacalone and V. Somà, *Evidence of the triaxial structure of ^{129}Xe at the Large Hadron Collider*, *Phys. Rev. Lett.* **128** (2022) no. 8 082301 [arXiv:2108.09578 [nucl-th]].
- [74] J. Jia, *Probing triaxial deformation of atomic nuclei in high-energy heavy ion collisions*, *Phys. Rev. C* **105** (2022) no. 4 044905 [arXiv:2109.00604 [nucl-th]].
- [75] ALICE collaboration, S. Acharya *et al.*, *Characterizing the initial conditions of heavy-ion collisions at the LHC with mean transverse momentum and anisotropic flow correlations*, *Phys. Lett. B* **834** (2022) 137393 [arXiv:2111.06106 [nucl-ex]].
- [76] ATLAS collaboration, G. Aad *et al.*, *Correlations between flow and transverse momentum in Xe+Xe and Pb+Pb collisions at the LHC with the ATLAS detector: A probe of the heavy-ion initial state and nuclear deformation*, *Phys. Rev. C* **107** (2023) no. 5 054910 [arXiv:2205.00039 [nucl-ex]].
- [77] N. Fortier, S. Jeon and C. Gale, *Comparisons and Predictions for Collisions of deformed ^{238}U nuclei at $\sqrt{s_{NN}} = 193$ GeV*, arXiv:2308.09816 [nucl-th].
- [78] E. G. D. Nielsen, F. K. Rømer, K. Gulbrandsen and Y. Zhou, *Generic multi-particle transverse momentum correlations as a new tool for studying nuclear structure at the energy frontier*, *Eur. Phys. J. A* **60** (2024) no. 2 38 [arXiv:2312.00492 [nucl-th]].
- [79] Z. Wang, J. Chen, H.-j. Xu and J. Zhao, *Systematic investigation of the nuclear multiple deformations in U+U collisions with A Multi-Phase Transport model*, arXiv:2405.09329 [nucl-th].
- [80] N. Fortier, S. Jeon and C. Gale, *Heavy-Ion Collisions as Probes of Nuclear Structure*, arXiv:2405.17526 [nucl-th].
- [81] E. Epelbaum, H.-W. Hammer and U.-G. Meissner, *Modern Theory of Nuclear Forces*, *Rev. Mod. Phys.* **81** (2009) 1773 [arXiv:0811.1338 [nucl-th]].
- [82] M. Piarulli and I. Tews, *Local Nucleon-Nucleon and Three-Nucleon Interactions Within Chiral Effective Field Theory*, *Front. in Phys.* **7** (2020) 245 [arXiv:2002.00032 [nucl-th]].
- [83] S. Elhatisari *et al.*, *Wave function matching for the quantum many-body problem*, arXiv:2210.17488 [nucl-th].
- [84] M. Frosini, T. Duguet and P. Tamagno, *Tensor factorization in ab initio many-body calculations: Triaxially-deformed (B) MBPT calculations in large bases*, arXiv:2404.08532 [nucl-th].
- [85] Z. H. Sun, A. Ekström, C. Forssén, G. Hagen, G. R. Jansen and T. Papenbrock, 2024. arXiv:2404.00058 [nucl-th].
- [86] B. S. Hu, Z. H. Sun, G. Hagen and T. Papenbrock, *Ab initio computations of strongly deformed nuclei around ^{80}Zr* , arXiv:2405.05052 [nucl-th].
- [87] J. Meija, T. B. Coplen, M. Berglund, W. A. Brand, P. D. Bièvre, M. Gröning, N. E. Holden, J. Irrgeher, R. D. Loss, T. Walczyk and T. Prohaska, *Isotopic compositions of the elements 2013 (iupac technical report)*, *Pure and Applied Chemistry* **88** (2016) no. 3 293. <https://doi.org/10.1515/pac-2015-0503>.
- [88] R. Pordes *et al.*, *The Open Science Grid*, *J. Phys. Conf. Ser.* **78** (2007) 012057.
- [89] I. Sfiligoi, D. C. Bradley, B. Holzman, P. Mhashilkar, S. Padhi and F. Wurthwein, *The pilot way to Grid resources using glideinWMS*, *WRI World Congress 2*

- (2009) 428.
- [90] C. Shen and B. Schenke, *Dynamical initial state model for relativistic heavy-ion collisions*, *Phys. Rev. C* **97** (2018) no. 2 024907 [[arXiv:1710.00881](#) [[nucl-th](#)]].
- [91] A. Bialas, A. Bzdak and V. Koch, *Stopped nucleons in configuration space*, *Acta Phys. Polon. B* **49** (2018) 103 [[arXiv:1608.07041](#) [[hep-ph](#)]].
- [92] C. Shen and B. Schenke, *Dynamical initialization and hydrodynamic modeling of relativistic heavy-ion collisions*, *Nucl. Phys. A* **982** (2019) 411 [[arXiv:1807.05141](#) [[nucl-th](#)]].
- [93] M. Okai, K. Kawaguchi, Y. Tachibana and T. Hirano, *New approach to initializing hydrodynamic fields and mini-jet propagation in quark-gluon fluids*, *Phys. Rev. C* **95** (2017) no. 5 054914 [[arXiv:1702.07541](#) [[nucl-th](#)]].
- [94] C. Shen, G. Denicol, C. Gale, S. Jeon, A. Monnai and B. Schenke, *A hybrid approach to relativistic heavy-ion collisions at the RHIC BES energies*, *Nucl. Phys. A* **967** (2017) 796 [[arXiv:1704.04109](#) [[nucl-th](#)]].
- [95] G. Giacalone, L. Yan, J. Noronha-Hostler and J.-Y. Ollitrault, *Skewness of elliptic flow fluctuations*, *Phys. Rev. C* **95** (2017) no. 1 014913 [[arXiv:1608.01823](#) [[nucl-th](#)]].
- [96] J. Jia, G. Giacalone and C. Zhang, *Separating the Impact of Nuclear Skin and Nuclear Deformation in High-Energy Isobar Collisions*, *Phys. Rev. Lett.* **131** (2023) no. 2 022301 [[arXiv:2206.10449](#) [[nucl-th](#)]].